Supporting Information

Cooperative Catalysis by Surface Lewis Acid/Silanol for
Selective Fructose Etherification on Sn-SPP Zeolite

Tyler R. Josephson*, Robert F. DeJaco, Swagata Pahari, Limin Ren, Qiang Guo, Michael Tsapatsis, J. Ilja Siepmann, Dionisios G. Vlachos, Stavros Caratzoulas

[1] *University of Delaware, Department of Chemical and Biomolecular Engineering*
*Harker Interdisciplinary Science and Engineering Laboratory, 221 Academy Street, Newark, DE  19716*

[2] *University of Minnesota, Department of Chemistry*
*139 Smith Hall, 207 Pleasant Street SE, Minneapolis, MN  55455*

[3] *University of Minnesota, Department of Chemical Engineering and Materials Science*
*151 Amundson Hall, 412 Washington Avenue SE, Minneapolis, MN  55455*

* Email for corresponding author: josep180@umn.edu

1. Additional reaction profiles on Sn-SPP
   a. Open fructose to furanose pathways
   b. Open fructose to hemiketal pathways
   c. Glucose isomerization to fructose pathway
2. Role of dispersion corrections on the reaction pathways
3. Free energy contributions to the reaction pathway
4. Comparison of stabilities of model oxonium intermediates in the gas phase
5. Detailed methods and results for Gibbs ensemble Monte Carlo simulations

**Pathway B**

| Open Fructose | Ring-Closing TS | Deprotonated Fructose | Reprotonation TS | Furanose |
|---|---|---|---|---|
| −0.9 | 8.1 | 7.3 | 13.6 | 6.7 |

**Pathway C**

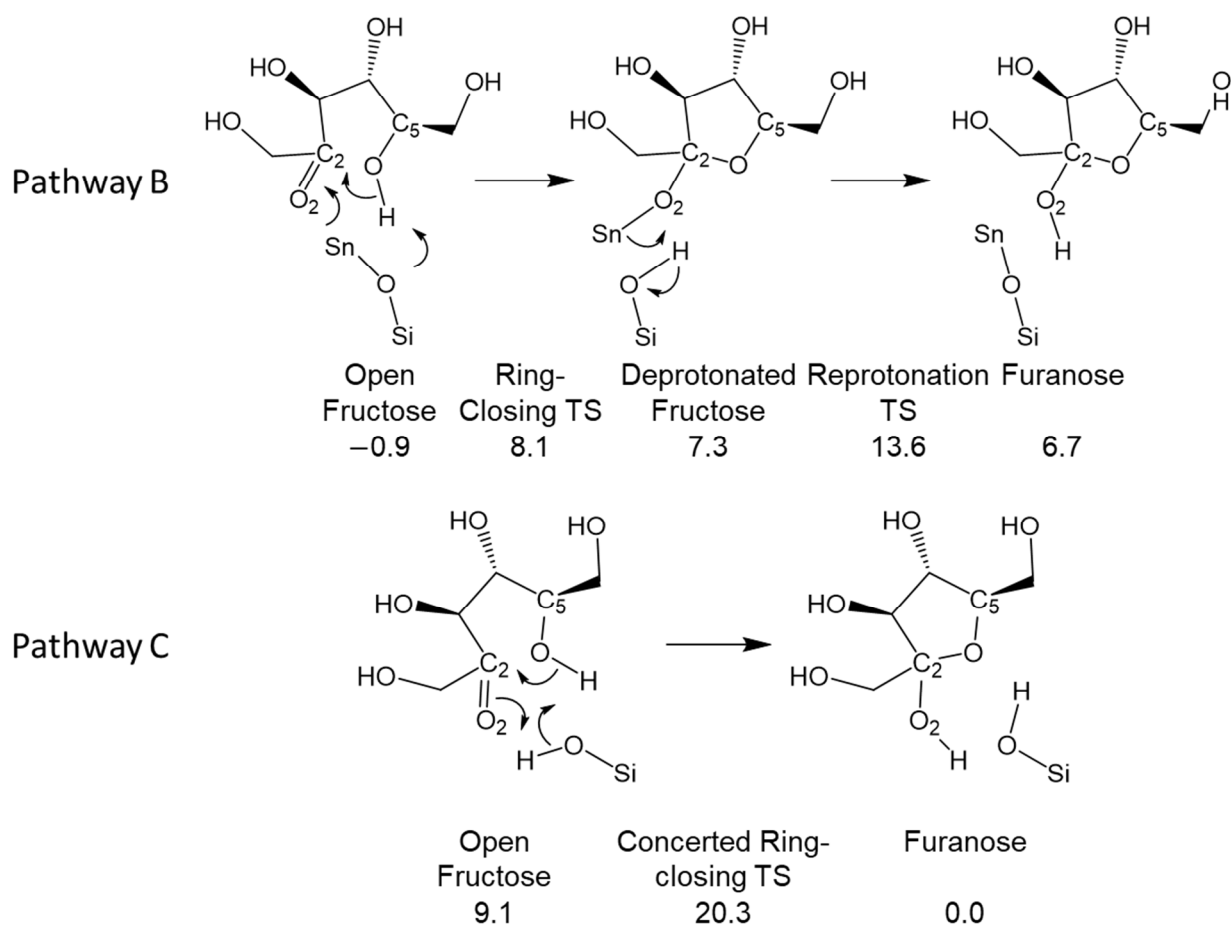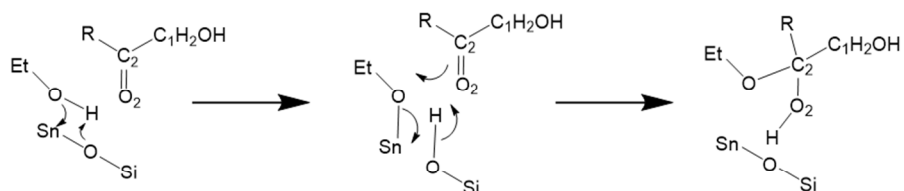| Open Fructose | Concerted Ring-closing TS | Furanose |
|---|---|---|
| 9.1 | 20.3 | 0.0 |

**Figure S1 - Hemiketalization pathways calculated for open fructose ring-closing to fructofuranose 2. Relative PBE-d3 electronic energies (kcal/mol) are reported with respect to the minimum furanose energy in Figure S2, Pathway C. PBE energies are reported in Table S1.**
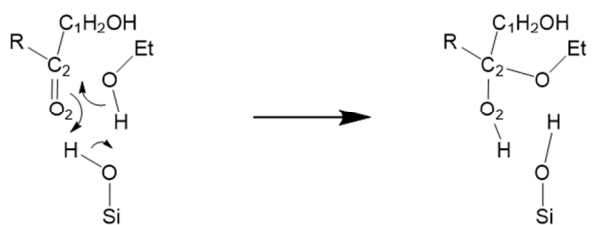
**Pathway A**



| Open Fructose | Deprotonation TS | Deprotonated EtOH | HemiK Formation TS | HemiK |
|---|---|---|---|---|
| −2.8 | 8.2 | 8.0 | 22.4 | 9.8 |

**Pathway B**
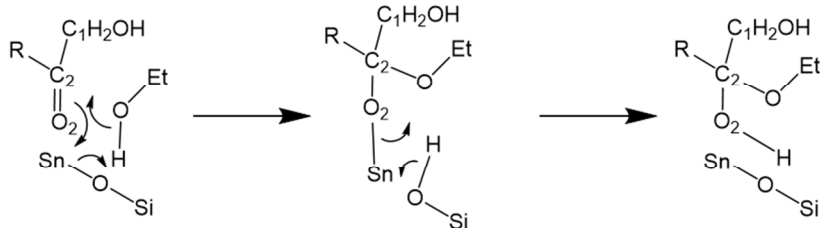


| Open Fructose | EtOH Addition TS | Deprotonated HemiK | Reprotonate HemiK TS | HemiK |
|---|---|---|---|---|
| 8.0 | 23.1 | 21.4 | 30.5 | 21.6 |

**Pathway C**



| Open Fructose | Concerted Hemiketalization TS | HemiK |
|---|---|---|
| 11.2 | 27.4 | 8.1 |

**Figure S2 - Hemiketalization pathways calculated for open fructose reaction to hemiketal 2. Relative PBE-d3 electronic energies (kcal/mol) are reported with respect to the minimum furanose energy in Figure S1, Pathway C. PBE energies are reported in Table S1. R = $C_4H_9O_4$ fragment of fructose**

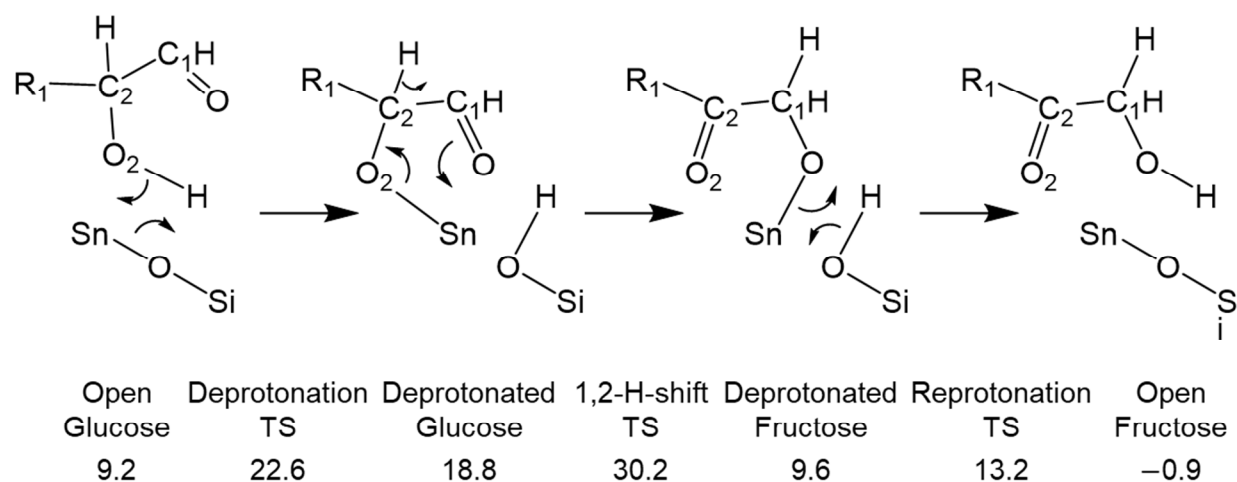| Open Glucose | Deprotonation TS | Deprotonated Glucose | 1,2-H-shift TS | Deprotonated Fructose | Reprotonation TS | Open Fructose |
|---|---|---|---|---|---|---|
| 9.2 | 22.6 | 18.8 | 30.2 | 9.6 | 13.2 | −0.9 |

Figure S3 - Glucose isomerization reaction pathway on Sn-SPP. Reaction follows bidentate reaction mechanism with a chelate-like intermediate. Relative PBE-d3 electronic energies (kcal/mol) are reported with respect to the minimum furanose energy in Figure S1, Pathway C. PBE energies are reported in Table S1. R = $C_4H_9O_4$ fragment of fructose/glucose.

Role of dispersion corrections on the reaction pathways

To compare the pathways with and without Grimme's D3 dispersion correction, we compared the energetics with and without the dispersion correction (Table S1). As expected, the electronic binding energies relative to gas phase are significantly weaker with PBE than with PBE-D3 (by ~20 kcal/mol). However, because we are investigating adsorption from solution phase, we have used Gibbs Ensemble Monte Carlo to estimate the free energies of transfer from solution. The OPLS and TraPPE force fields implicitly include dispersion via the procedure in which they were fit to experiment.

While dispersion slightly affects the relative energy differences among intermediates and transition states in the reaction pathways (mean deviation of $-1.2$ kcal/mol and mean absolute deviation of 2.6 kcal/mol), both methods find the same pathway to be most favorable. According to PBE-d3, the favored mechanism (HemiK $S_N1$ with SiOH) has a maximum TS energy that is 4.2 kcal/mol lower than the next-lowest pathway on Sn-SPP (HemiK $S_N1$ without SiOH), and 8.2 kcal/mol lower than the pathway on Sn-Beta. For PBE without dispersion, these differences are accentuated; HemiK $S_N1$ with SiOH is 9.3 kcal/mol lower than the next-lowest pathway on Sn-SPP, and 12.0 kcal/mol lower than the pathway on Sn-Beta.

Tables S1-S4 also provides an inventory of the energetics of the geometries included in the Supporting Information.

| Fig S1 | PBE | | PBE-D3 | |
|---|---|---|---|---|
| | Binding E | Relative E | Binding E | Relative E |
| PathwayB_1_OpenFructose1 | −28.1 | −0.2 | −53.9 | -0.9 |
| PathwayB_2_Ring-closingTS | −17.3 | 10.6 | −45.0 | 8.1 |
| PathwayB_3_DeprotonatedFuranose | −18.2 | 9.8 | −45.8 | 7.3 |
| PathwayB_4_ReprotonationTS | −11.7 | 16.2 | −39.4 | 13.6 |
| PathwayB_5_Furanose2 | −21.7 | 6.3 | −46.4 | 6.7 |
| | | | | |
| PathwayC_1_OpenFructose1 | −19.6 | 8.3 | −43.9 | 9.1 |
| PathwayC_2_ConcertedRing-closingTS | −6.2 | 21.7 | −32.8 | 20.3 |
| PathwayC_3_Furanose2 | −28.0 | 0.0 | −53.1 | 0.0 |
| | | | | |
| **Fig S2** | | | | |
| PathwayA_1_OpenFructose1 | −28.2 | -0.3 | −55.8 | −2.8 |
| PathwayA_2_DeprotonationTS | −14.2 | 13.8 | −44.9 | 8.2 |
| PathwayA_3_DeprotonatedEtOH | −14.9 | 13.1 | −45.1 | 8.0 |
| PathwayA_4_HemiketalFormationTS | 1.4 | 29.3 | −30.7 | 22.4 |
| PathwayA_5_Hemiketal3 | −14.6 | 13.3 | −43.3 | 9.8 |
| | | | | |
| PathwayB_1_OpenFructose1 | −20.0 | 8.0 | −45.1 | 8.0 |
| PathwayB_2_EtOHAdditionTS | 0.5 | 28.5 | −29.9 | 23.1 |
| PathwayB_3_DeprotonatedHemiketal | −3.0 | 25.0 | −31.6 | 21.4 |
| PathwayB_4_ReprotonateHemiketalTS | 7.0 | 34.9 | −22.6 | 30.5 |
| PathwayB_5_Hemiketal3 | −5.1 | 22.8 | −31.5 | 21.6 |
| | | | | |
| PathwayC_1_OpenFructose1 | −16.6 | 11.4 | −41.8 | 11.2 |
| PathwayC_2_ConcertedRingClosingTS | 2.7 | 30.7 | −25.6 | 27.4 |
| PathwayC_3_Hemiketal3 | −19.6 | 8.4 | −44.9 | 8.1 |
| | | | | |
| **Fig S3** | | | | |
| Isom1_OpenGLU | −19.4 | 8.6 | −43.8 | 9.2 |
| Isom2_DeprotonationTS | −4.3 | 23.6 | −30.5 | 22.6 |
| Isom3_DeprotonatedGLU | −8.8 | 19.1 | −34.3 | 18.8 |
| Isom4_1,2-H-shiftTS | 3.1 | 31.1 | −22.9 | 30.2 |
| Isom5_DepronatedFRU | −18.7 | 9.2 | −43.4 | 9.6 |
| Isom6_ReprotonationTS | −13.2 | 14.7 | −39.8 | 13.2 |
| Isom7_OpenFru | −28.1 | -0.2 | −53.9 | −0.9 |

**Table S2 – Comparing influence of dispersion on reaction energetics. Electronic binding energies are calculated relative to infinitely separated fructose, ethanol, and Sn-SPP.**

| | PBE | | PBE-D3 | |
|---|---|---|---|---|
| FurSN2 without SiOH | Binding E | Relative E | Binding E | Relative E |
| FurSN2_2_1_Furanose | −22.3 | 5.6 | −42.5 | 10.5 |
| FurSN2_2_2_KetalizationTS | 23.9 | 51.8 | −3.6 | 49.5 |
| FurSN2_2_3_Ketal+H+OH | −13.4 | 14.5 | −38.4 | 14.7 |
| FurSN2_2_4_WaterFormationTS | −4.7 | 23.2 | −29.7 | 23.4 |
| FurSN2_2_5_Ketal+H2O | −21.4 | 6.6 | −44.4 | 8.7 |
| FurSN1 with SiOH | | | | |
| FurSN2_1_1_Furanose | −22.8 | 5.2 | −42.4 | 10.7 |
| FurSN2_1_2_KetalizationTS | 20.2 | 48.1 | -2.8 | 50.2 |
| FurSN2_1_3_Ketal | −16.5 | 11.4 | −37.9 | 15.1 |
| FurSN1 without SiOH | | | | |
| FurSN1_2_1_Furanose | −25.6 | 2.3 | −46.0 | 7.0 |
| FurSN1_2_2_DehydrationTS | 14.0 | 42.0 | -8.9 | 44.2 |
| FurSN1_2_3_Int1 | −1.2 | 26.8 | −25.6 | 27.5 |
| FurSN1_2_4_KetalizationTS | 8.4 | 36.4 | −18.0 | 35.1 |
| FurSN1_2_5_Ketal | 3.3 | 31.2 | −20.5 | 32.5 |
| FurSN1 with SiOH | | | | |
| FurSN1_1_1_Furanose | −23.4 | 4.6 | −51.0 | 2.1 |
| FurSN1_1_2_DehydrationTS | 5.7 | 33.6 | −24.0 | 29.1 |
| FurSN1_1_3_Int1 | −0.9 | 27.0 | −29.5 | 23.6 |
| FurSN1_1_4_KetalizationTS | 12.6 | 40.5 | −16.8 | 36.2 |
| FurSN1_1_5_Ketal | −12.5 | 15.4 | −35.5 | 17.5 |
| HemiKSN1 without SiOH | | | | |
| HemiKSN1_1_1_Hemiketal | −16.9 | 11.1 | −45.8 | 7.2 |
| HemiKSN1_1_2_DeprotonationTS | 5.2 | 33.2 | −25.2 | 27.9 |
| HemiKSN1_1_3_DeprotonatedO2 | 1.9 | 29.9 | −28.7 | 24.3 |
| HemiKSN1_1_4_DehydrationTS | 12.4 | 40.4 | −19.2 | 33.8 |
| HemiKSN1_1_5_Int1b | 7.1 | 35.1 | −21.4 | 31.7 |
| HemiKSN1_1_6_ReorganizationTS | 8.5 | 36.4 | −21.0 | 32.0 |
| HemiKSN1_1_7_Int1 | 2.8 | 30.8 | −24.0 | 29.1 |
| HemiKSN1_1_8_RingClosingTS | 8.4 | 36.4 | −19.1 | 33.9 |
| HemiKSN1_1_9_Ketal | −15.5 | 12.4 | −35.2 | 17.8 |
| HemiKSN1 with SiOH | | | | |
| HemiKSN1_2_1_Hemiketal | −21.0 | 6.9 | −46.8 | 6.3 |
| HemiKSN1_2_2_DehydrationTS | 3.2 | 31.1 | −23.4 | 29.7 |
| HemiKSN1_2_3_Int1b | −1.9 | 26.0 | −27.2 | 25.9 |
| HemiKSN1_2_4_ReorganizationTS | −0.9 | 27.1 | −28.2 | 24.9 |
| HemiKSN1_2_5_Int1 | −6.0 | 22.0 | −33.5 | 19.5 |
| HemiKSN1_2_6_RingClosingTS | 0.5 | 28.4 | −28.7 | 24.4 |
| HemiKSN1_2_7_Ketal | −10.5 | 17.4 | −36.6 | 16.5 |

**Table S3 – Comparing influence of dispersion on reaction energetics for glucose acetalization and hemiacetalization. Electronic binding energies are calculated relative to infinitely separated fructose, ethanol, and Sn-SPP.**

| Glucose Acetalization | PBE | | PBE-D3 | |
| --- | --- | --- | --- | --- |
| | Binding E | Relative E | Binding E | Relative E |
| GluA1_Hemiacetal | −20.4 | 7.6 | −40.4 | 12.7 |
| GluA2_DehydrationTS | 11.1 | 39.0 | −13.4 | 39.6 |
| GluA3_Int | 10.7 | 38.6 | −13.8 | 39.2 |
| GluA5_Glucoside | 12.6 | 40.6 | −11.7 | 41.4 |
| GluA5_RingCloseTS | −22.3 | 5.6 | −41.5 | 11.5 |
| | | | | |
| Hemiacetalization | | | | |
| GluAOpenGLU | −10.7 | 17.3 | −38.4 | 14.7 |
| GluAHemiacetalizationTS | −10.5 | 17.5 | −39.7 | 13.4 |
| GluADeprotonatedHemiacetal | −15.7 | 12.3 | −44.8 | 8.2 |
| GluAReprotonationTS | −6.8 | 21.1 | −36.6 | 16.5 |
| GluAHemiAcetalb | −12.7 | 15.3 | −40.6 | 12.5 |
| | | | | |
| GluAOpenGLUb | −6.9 | 21.0 | −32.2 | 20.9 |
| GluAPyranoseRingOpening | −3.5 | 24.5 | −30.4 | 22.7 |
| GluAPyranose | −22.2 | 5.7 | −46.5 | 6.5 |

**Table S4 – Comparing influence of dispersion on reaction energetics for reactions on Sn-Beta. Electronic binding energies are calculated relative to infinitely separated fructose, ethanol, and Sn-Beta.**

| Sn-Beta | PBE | | PBE-D3 | |
| --- | --- | --- | --- | --- |
| | Binding E | Relative E | Binding E | Relative E |
| BEA_0_Furanose | −19.8 | 0.0 | −55.8 | 0.0 |
| BEA_1_Furanose | −8.3 | 11.4 | −46.4 | 9.4 |
| BEA_2_Furanose_Deprotonation_TS | −2.1 | 17.7 | −40.7 | 15.1 |
| BEA_3_DP_Furanose | −11.2 | 8.5 | −48.9 | 7.0 |
| BEA_4_Ring_Opening_TS | −3.3 | 16.5 | −41.9 | 13.9 |
| BEA_5_Open_Fructose | −15.9 | 3.9 | −53.4 | 2.4 |
| BEA_6_Hemiketalization_TS | 3.6 | 23.4 | −34.4 | 21.5 |
| BEA_7_Open_Fructose | −6.3 | 13.4 | −41.9 | 14.0 |
| BEA_8_Hemiketal | −3.4 | 16.4 | −39.9 | 15.9 |
| BEA_9_Hemiketal | 11.9 | 31.7 | −27.6 | 28.2 |
| BEA_10_Dehydration_TS | 23.3 | 43.1 | −17.9 | 37.9 |
| BEA_11_Int | 15.2 | 34.9 | −25.8 | 30.0 |
| BEA_12_Ring_Closing_TS | 15.5 | 35.3 | −26.0 | 29.8 |
| BEA_13_Ketal | 2.0 | 21.8 | −36.9 | 18.9 |

**Table S5 – Comparing influence of dispersion on reaction energetics for Sn site substitutions. T8 remains the global minimum, although the relative differences change slightly for the other T sites.**

| T Site | PBE E | T Site | PBD-d3 E |
|--------|-------|--------|----------|
| 8 | 0.00 | 8 | 0 |
| 9 | 0.31 | 10 | 0.20 |
| 10 | 0.54 | 9 | 0.72 |
| 7 | 1.22 | 7 | 0.79 |
| 12 | 2.54 | 12 | 1.96 |
| 11 | 4.29 | 11 | 3.75 |
| 4 | 5.30 | 4 | 3.90 |
| 3 | 7.85 | 3 | 5.54 |
| 1 | 7.95 | 1 | 6.90 |
| 5 | 8.62 | 2 | 7.75 |
| 2 | 9.12 | 5 | 8.35 |
| 6 | 12.3 | 6 | 10.5 |

Free energy contributions to the reaction pathway

**Table S6 – Binding potential and free energies calculated using the harmonic approximation, shifted according to the Gibbs Ensemble Monte Carlo (GEMC) simulations. All energies are given in kcal/mol.**

|  | Binding E | Binding G | Relative Binding G | GEMC-shifted G |
|---|---|---|---|---|
| Sn-SPP |  |  |  |  |
| Furanose (sol) |  |  |  | 0 |
| Furanose (ads) | −53.1 | −52.7 | 0 | 0.8 |
| Open FRU | −55.8 | −55.8 | −3.1 | −2.3 |
| HemiK TS | −30.7 | −30.2 | 22.5 | 23.3 |
| HemiK | −46.8 | −45.4 | 7.3 | 8.1 |
| Dehydration TS | −23.4 | −24.1 | 28.6 | 29.4 |
| Int 1 | −27.2 | −31.7 | 21.0 | 21.8 |
| Rearrange TS | −28.2 | −29.6 | 23.1 | 23.9 |
| Int 2 | −33.5 | −33.6 | 19.1 | 19.9 |
| Ring Close TS | −28.7 | −29.5 | 23.2 | 24 |
| Ketal (ads) | −36.6 | −37.2 | 15.5 | 16.3 |
| Sn-Beta |  |  |  |  |
| Furanose (sol) |  |  |  | 0 |
| Furanose (ads) | −55.8 | −55.8 | 0 | 3 |
| Open FRU | −53.4 | −52.8 | 3.0 | 6.0 |
| HemiK TS | −34.4 | −35.9 | 19.9 | 22.9 |
| HemiK 1 | −39.9 | −40.9 | 14.9 | 17.9 |
| HemiK 2 | −27.6 | −25.2 | 30.6 | 33.6 |
| Dehydration TS | −17.9 | −19.2 | 36.6 | 39.6 |
| Int 1 | −25.8 | −27.2 | 28.6 | 31.6 |
| Ring Close TS | −26.0 | −27.2 | 28.6 | 31.6 |
| Ketal (ads) | −36.9 | −37.2 | 18.6 | 21.6 |

Gas-phase stability of model oxonium intermediates

Gas-phase oxonium stability was investigated using Gaussian 09, at the M062X/aug-cc-pvdz theory level. While a 5-ring hemiketal is only 0.7 kcal/mol more stable than its 6-ring counterpart, the hemiketal hydroxyl has significantly greater proton affinity than the hemiacetal hydroxyl, and the dehydrated oxonium for the hemiketal is 13.3 kcal/mol more stable. The same trends are also observed for the linear hemiketal and hemiacetal tested.

So, hemiketals are more reactive for $SN_1$ mechanisms, both due to increased proton affinity and increased oxonium stability.
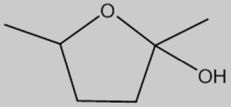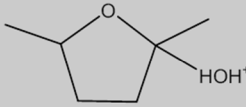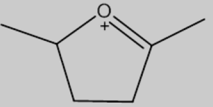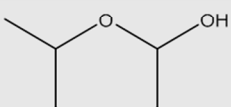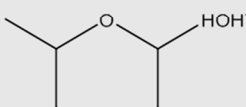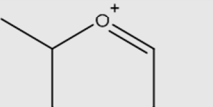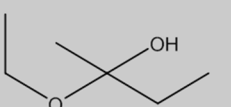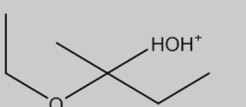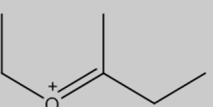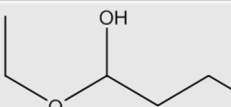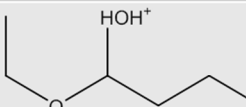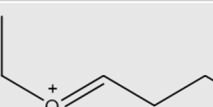
| | Intermediate | Protonated OH | Water removed |
|---|---|---|---|
| 5-ring hemiketal | 1a<br>Rel. ΔG = 0 | 1b<br>PA: 213.4 | 1c<br>Rel. ΔG = 0 |
| 6-ring hemiacetal | 2a<br>Rel. ΔG = 0.7 | 2b<br>PA: 201.0 | 2c<br>Rel. ΔG = 13.3 |
| Linear hemiketal | 3a<br>Rel. ΔG = 0 | 3b<br>PA: 212.0 | 3c<br>Rel. ΔG = 0 |
| Linear hemiacetal | 4a<br>Rel. ΔG = 4.2 | 4b<br>PA: 203.1 | 4c<br>Rel. ΔG = 14.2 |

**Figure S4 – Gas-phase calculations for model hemiketals and hemiacetals. Free energies are reported in kcal/mol. Relative free energies for 1a-c and 2a-c are reported with respect to 1a and 1c, and for 3a-c and 4a-c with respect to 3a and 3c.**

Gibbs ensemble Monte Carlo simulation details

Monte Carlo (MC) simulations in the isobaric–isothermal version of the Gibbs ensemble[1–3] were employed at $T$ = 363 K and $p$ = 1.7 bar with three simulation boxes in thermodynamic (but not physical) contact representing a zeolite phase, a vapor box, and a solution phase. The set of trial moves included rigid-body translations and rotations around the center-of-mass (COM) for all sorbates, and coupled-decoupled[4] configurational bias Monte Carlo[5–7] (CD-CBMC) moves for ethanol. CD-CBMC strategies were also employed for particle transfer moves between two phases[6,8]. To facilitate particle transfer moves of fructose between the liquid and zeolite boxes, an intermediate ideal-gas box[9] and identity switch moves[10,11] involving pairs of impurity molecules with scaled non-bonded parameters (8 variants were used) and fructose were used. A suitable volume of the vapor box was achieved by means of a fixed amount of ideal (i.e., noninteracting) particles. Volume moves were performed on all boxes except those representing a zeolite phase.

**Table S7 – Nonbonded parameters used for Sn atoms or those on silanol groups or stannanol groups in the molecular simulations.**

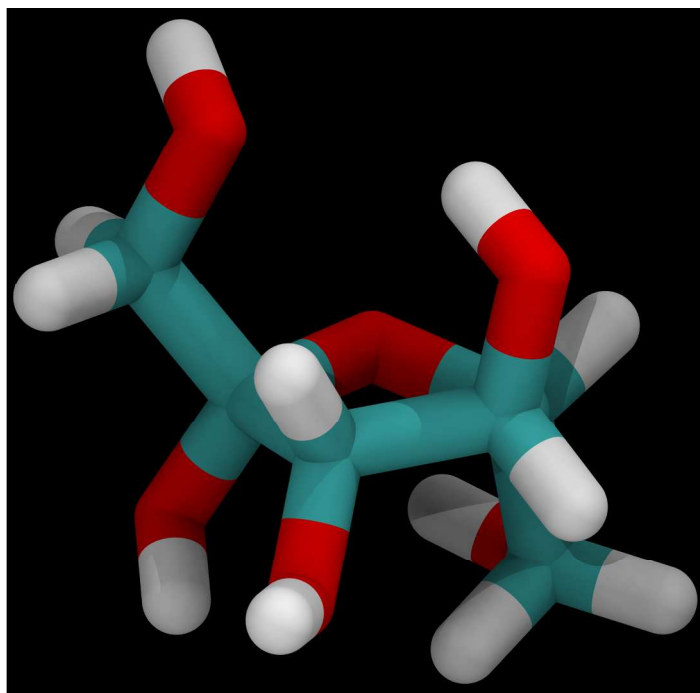| Atom | Zeolite | $\varepsilon/k_B$ [K] | $\sigma$ [Å] | q [e] |
|---|---|---|---|---|
| Si (silanol) | Sn-BEA or Sn-SPP | 22.0 | 2.30 | 1.429 |
| Sn | Sn-BEA | 40.6 | 2.80 | 1.555 |
| O (silanol OH) | Sn-BEA or Sn-SPP | 93.0 | 3.02 | −0.739 |
| O (stannanol OH) | Sn-BEA | 93.0 | 3.02 | −0.887 |
| H (silanol OH) | Sn-BEA or Sn-SPP | 0. | 0. | 0.435 |
| H (stannanol OH) | Sn-BEA | 0. | 0. | 0.457 |
| Sn | Sn-SPP | 40.6 | 2.80 | 1.5 |

**Figure S5 – Sample configuration of fructose used in semi-flexible representation in Gibbs ensemble molecular simulations.**

Ethanol was modeled using the united-atom version of the TraPPE force field[12,13]. The all-atom version of the Optimized Potentials for Liquid Simulations (OPLS-AA) force field was used for fructose[14]. Framework Si and O atoms were modeled using the Transferable Potentials for Phase Equilibria (TraPPE) force field for zeolites[15]. The Lennard-Jones (LJ) parameters for O and H and the partial charges on silanol groups were adopted from previous work[16,17]. The ratios for the LJ parameters for Sn and Si were set to be those of Xe and Ar (see Table S3). The partial charges of Sn, O, and H on the stannanol groups were obtained by scaling them from the Si, O, and H on the silanol groups according the ratio of CM5 charges obtained from DFT calculations of $H_3SiOH$ and $H_3SnOH$ using M062x/aug-cc-pVDZ in SMD n-octanol solvent[18] while maintaining charge-neutrality, resulting in the charges shown in Table S3. Fructose (see Figure S5), silanol groups, and stannanol groups were modeled as semi-flexible; that is, they were represented as rigid with flexible protons on hydroxyl groups.

Given the large size of the mesopores[19] and for consistency with the electronic structure calculations, Sn-SPP was modeled as a 2-nm thick sheet (one unit cell in the *b*-direction) surrounded by void space. The structure of Sn-SPP nanosheet was initialized from the idealized MFI framework structure[20] and optimized using the DFT methods described in the main text, and the structure of the optimized Sn-Beta zeolite was obtained from our previous screening of open site geometries[21]. The unit cell of Sn-BEA was replicated to form a 3 by 3 by 2 supercell with dimensions of 3.79 by 3.79 by 5.24 nm, and Sn-SPP nanosheet was replicated twice in the *a*-direction and three times in the *c*-direction to form a supercell of 3.94 by 6.00 by 4.02 nm. The Si/Sn ratios for the simulated Sn-BEA and Sn-SPP structures are 63 and 79, respectively, which are enriched in Sn by about a factor of 2 with respect to the experimental Si/Sn ratios of 125 and 186, respectively.

The total number of molecules $N_{tot}$, consisted of 15 fructose molecules, 8 impurity molecules, and 700 or 1000 ethanol molecules for the systems with Sn-Beta or Sn-SPP, respectively. Production periods ranged from 200,000 to 600,000 Monte Carlo Cycles (MCCs) with eight independent simulations, where each MCC consists of $N_{tot}$ randomly selected trial moves.

The results obtained directly from the simulations are presented in Table S3, and simulation snapshots are shown for the sample adsorbed configurations in Figures S6 and S7. In each case, the zeolite was nearly saturated with ethanol; however, the number of fructose molecules in the Sn-SPP simulation box was considerably higher than in Sn-Beta. To compensate for the difference in Sn content between simulation and experiment, the number density ratio $\rho_{FRU,zeo}/\rho_{FRU,sol}$ was multiplied by $(Si/Sn)_{exp}$ / $(Si/Sn)_{sim}$. In addition, the difference in mesopore volume fraction between this model (67%) and typical SPP zeolite samples (which range from 38 to 55 % mesopore volume[22]) causing an additional shift of 0.3 to 0.5 kcal/mol (see Table S4). Applying these corrections and using a mesopore volume fraction of 55% gives free energies of transfer onto the Sn sites, which are 0.8 ± 0.6 kcal/mol for Sn-SPP and 3 ± 1.2 kcal/mol for Sn-Beta. While these corrections help to ensure the simulations most closely resemble the experiment, nonetheless, they do not significantly affect the overall reaction profiles, which are dominated by much more significant reaction barriers.

**Table S3 – Gibbs ensemble simulation results. Uncertainties are reported as the 95% confidence intervals estimated by multiplying the standard error of the mean of eight independent simulations by a factor of 2.4**

| Zeolite | Total molecules | | Equilibrium Fructose concentration in solution [g/mL] | Number adsorbed in simulation box representing zeolite | | $\Delta G_{transfer, FRU}$ (kcal/mol) |
|---|---|---|---|---|---|---|
| | $N_{FRU}$ | $N_{EtOH}$ | $C$ | $N_{FRU}$ | $N_{EtOH}$ | Entire liquid box to entire zeolite box |
| **Sn-SPP** $(Si/Sn)_{sim}$ = 79 $(Si/Sn)_{exp}$ = 186 | 15 | 1000 | 0.027 ± 0.007 | 5 ± 1.6 | 638 ± 3 | 0.4 ± 0.4 |
| **Sn-Beta** $(Si/Sn)_{sim}$ = 63 $(Si/Sn)_{exp}$ = 125 | 15 | 700 | 0.081 ± 0.004 | 0.6 ± 0.4 | 209 ± 0.9 | 3 ± 1.7 |

**Table S8 - Free energies of transfer from solution to the surface of SPP**

| Zeolite | Free energy of transfer from solution to zeolite, adjusted for difference between Si/Sn ratio between simulation and experiment |
|---|---|
| Sn-SPP (volume fraction 38%) | 0.6 ± 0.6 kcal/mol |
| Sn-SPP (volume fraction 44%) | 0.7 ± 0.6 kcal/mol |

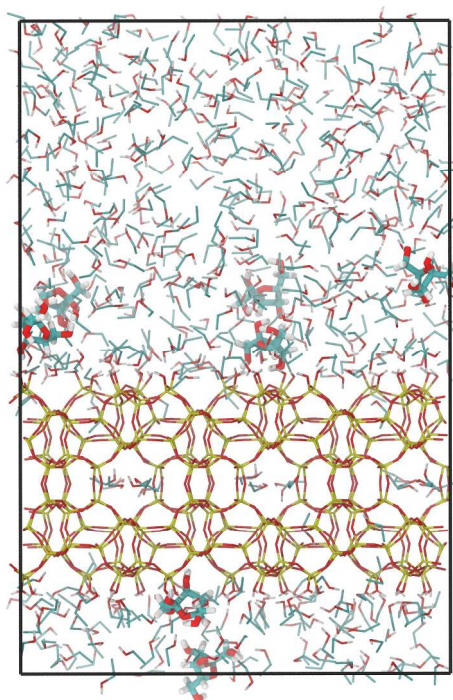| Sn-SPP (volume fraction 55%) | 0.8 ± 0.6 kcal/mol |
| Sn-SPP (simulated volume fraction) | 1.1 ± 0.6 kcal/mol |



**Figure S6 – Horizontal view of fructose and ethanol adsorbed onto Sn-SPP, as predicted by Gibbs ensemble Monte Carlo Simulations. Fructose molecules are emphasized with a tube representation, while the zeolite framework and ethanol molecules are drawn as lines.**
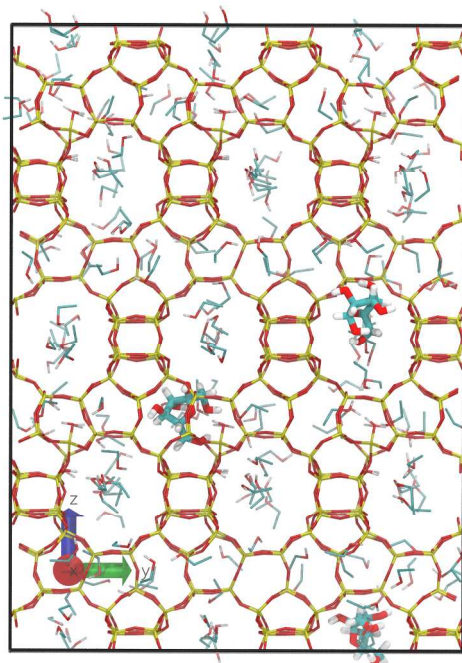
**Figure S7 – Views of the z-y plane of Sn-Beta, with fructose and ethanol adsorbed. Fructose molecules are emphasized with a tube representation, while the zeolite framework and ethanol molecules are drawn as lines.**
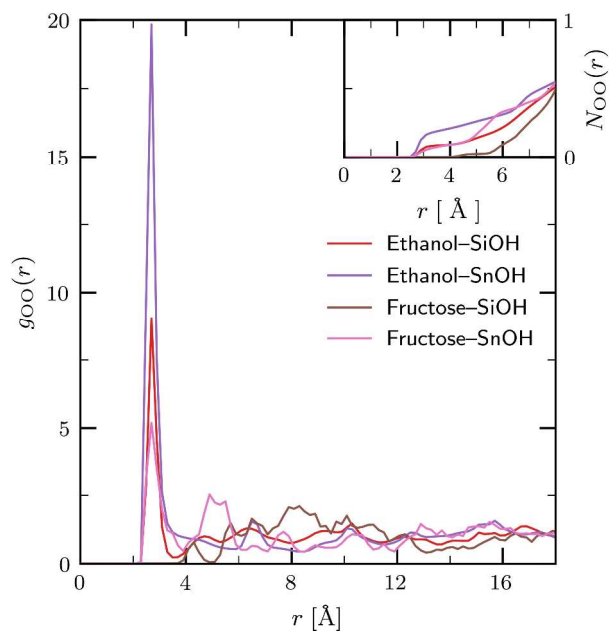


**Figure S8 – Oxygen—oxygen radial distribution functions and (inset) corresponding number integrals in Sn-BEA as determined from the Monte Carlo simulations in the Gibbs ensemble. The oxygens for silanols (SiOH) and stannanols (SnOH) are those on the corresponding hydroxyl groups.**

The competition for adsorption of fructose and ethanol to the active site of Sn-Beta is observed in Figure S8 by means of the radial distribution functions (RDFs) and corresponding number integrals (inset). Both sorbates prefer to adsorb near stannanol oxygens than silanol oxygens. Ethanol prefers to adsorb closer

to both silanol oxygens and stannanol oxygens than fructose does. This is attributed to ethanol's smaller size and much smaller number of oxygens. This reveals significant competition between ethanol and fructose for adsorption near the active sites in Sn-Beta, like that observed for Sn-SPP.

(1)     Panagiotopoulos, A. Z. Direct Determination of Phase Coexistence Properties of Fluids by Monte Carlo Simulation in a New Ensemble. *Mol. Phys.* **1987**, *61*, 813–826.

(2)     Panagiotopoulos, A. Z.; Quirke, N.; Stapleton, M.; Tildesley, D. J. Phase Equilibria by Simulation in the Gibbs Ensemble Alternative Derivation, Generalization and Application to Mixture and Membrane Equilibria. *Mol. Phys.* **1988**, *63*, 527–545.

(3)     Smit, B.; De Smedt, P.; Frenkel, D. Computer Simulations in the Gibbs Ensemble. *Mol. Phys.* **1989**, *68*, 931–950.

(4)     Martin, M. G.; Siepmann, J. I. Novel Configurational-Bias Monte Carlo Method for Branched Molecules. Transferable Potentials for Phase Equilibria. 2. United-Atom Description of Branched Alkanes. *J. Phys. Chem. B* **1999**, *103*, 4508–4517.

(5)     Siepmann, J. I.; Frenkel, D. Configurational Bias Monte Carlo: A New Sampling Scheme for Flexible Chains. *Mol. Phys.* **1992**, *75*, 59–70.

(6)     Mooij, G. C. A. M.; Frenkel, D.; Smit, B. Direct Simulation of Phase Equilibria of Chain Molecules. *J. Phys. Condens. Matter* **1992**, *4*, L255–L259.

(7)     De Pablo, J. J. Simulation of Phase Equilibria for Chain Molecules. *Fluid Phase Equilib.* **1995**, *104*, 195–206.

(8)     Laso, M.; de Pablo, J.; Suter, U. Simulation of Phase Equilibra for Chain Molecules. *J. Chem. Phys.* **1992**, *97*, 2817.

(9)     Lopes, J. N. C.; Tildesley, D. J. Three-Phase Osmotic Equilibria Using the Gibbs Ensemble Simulation Method. *Mol. Phys.* **2000**, *98*, 769–772.

(10)    Martin, M. G.; Siepmann, J. I.; Fields, F. Predicting Multicomponent Phase Equilibria and Free Energies of Transfer for Alkanes by Molecular Simulation. *J. Am. Chem. Soc.* **1997**, *119*, 8921–8924.

(11)    Bai, P.; Siepmann, J. I.; Deem, M. W. Adsorption of Glucose into Zeolite Beta from Aqueous Solution. *AIChE J.* **2013**, *59*, 3523–3529.

(12)    Martin, M. G.; Siepmann, J. I. Transferable Potentials for Phase Equilibria. 1. United-Atom Description of n -Alkanes. *J. Phys. Chem. B* **1998**, *102*, 2569–2577.

(13)    Chen, B.; Potoff, J. J.; Siepmann, J. I. Monte Carlo Calculations for Alcohols and Their Mixtures with Alkanes. Transferable Potentials for Phase Equilibria. 5. United-Atom Description of Primary, Secondary, and Tertiary Alcohols. *J. Phys. Chem. B* **2001**, *105*, 3093--3104.

(14)    Damm, W.; Frontera, A.; Tirado-Rives, J.; Jorgensen, W. L. OPLS All-Atom Force Field for Carbohydrates. *J. Comput. Chem.* **1997**, *18*, 1955–1970.

(15)  Bai, P.; Tsapatsis, M.; Siepmann, J. I. TraPPE-Zeo: Transferable Potentials for Phase Equilibria Force Field for All-Silica Zeolites. *J. Phys. Chem. C* **2013**, *117*, 24375–24387.

(16)  Rafferty, J. L.; Siepmann, J. I.; Schure, M. R. Influence of Bonded-Phase Coverage in Reversed-Phase Liquid Chromatography via Molecular Simulation. I. Effects on Chain Conformation and Interfacial Properties. *J. Chromatogr. A* **2008**, *1204*, 11–19.

(17)  Farzaneh, A.; DeJaco, R. F.; Ohlin, L.; Holmgren, A.; Siepmann, J. I.; Grahn, M. Comparative Study of the Effect of Defects on Selective Adsorption of Butanol from Butanol/Water Binary Vapor Mixtures in Silicalite-1 Films. *Langmuir* **2017**, *33*, 8420–8427.

(18)  Marenich, A. V; Cramer, C. J.; Truhlar, D. G.; Marenich Cramer, Christopher J., and Truhlar, Donald G., A. V. Universal Solvation Model Based on Solute Electron Density and on a Continuum Model of the Solvent Defined by the Bulk Dielectric Constant and Atomic Surface Tensions. *J. Phys. Chem. B* **2009**, *113*, 6378–6396.

(19)  Zhang, X.; Liu, D.; Xu, D.; Asahina, S.; Cychosz, K. A.; Agrawal, K. V.; Al Wahedi, Y.; Bhan, A.; Al Hashimi, S.; Terasaki, O.; et al. Synthesis of Self-Pillared Zeolite Nanosheets by Repetitive Branching. *Science.* **2012**, *336*, 1684–1687.

(20)  Baerlocher, C.; McCusker, L. B. Database of Zeolite Structures http://www.iza-structure.org/databases/, **2016**.

(21)  Josephson, T. R.; Jenness, G. R.; Vlachos, D. G.; Caratzoulas, S. Distribution of Open Sites in Sn-Beta Zeolite. *Microporous Mesoporous Mater.* **2017**, *245*, 45–50.

(22)  Bai, P.; Olson, D. H.; Tsapatsis, M.; Siepmann, J. I. Understanding the Unusual Adsorption Behavior in Hierarchical Zeolite Nanosheets. *Chem. Phys. Chem.* **2014**, *15*, 2225–2229.